ACS APPLIED NANO MATERIALS

www.acsanm.org

Article

Controlled Nanopore Sizes in Supraparticle Supports for Enhanced Propane Dehydrogenation with GaPt SCALMS Catalysts

Nnamdi Madubuko,[○] Umair Sultan,[○] Simon Carl, Daniel Lehmann, Xin Zhou, Alexander Soegaard, Nicola Taccardi, Benjamin Apeleo Zubiri, Susanne Wintzheimer, Erdmann Spiecker, Marco Haumann,* Nicolas Vogel,* and Peter Wasserscheid*

Cite This: *ACS Appl. Nano Mater.* 2024, 7, 24356−24367

Read Online

ACCESS | Metrics & More | Article Recommendations | Supporting Information

ABSTRACT: The efficient immobilization of GaPt liquid metal alloy droplets onto tailored supports improves catalytic performance by preventing coalescence and subsequent loss of active surface area. Herein, we use tailored supraparticle (SP) supports with controlled nanopores to systematically study the influence of pore sizes on the catalytic stability of GaPt supported catalytically active liquid metal solution (SCALMS) in propane dehydrogenation (PDH). Initially, GaPt droplets were prepared via an atom-efficient and scalable ultrasonication method with recycling loops to yield droplets <300 nm. Subsequently, these droplets were immobilized onto SiO_2-based SPs with controlled pore sizes ranging from 45 to 320 nm. Catalytic evaluations in PDH revealed that GaPt immobilized on SPs with larger pores demonstrated superior stability over 15 h time-on-stream evidenced by reduced deactivation rates from 0.046 to 0.026 h^{-1}. Nanocomputed tomography and identical location SEM confirmed the successful immobilization of GaPt droplets within the interstitial sites formed by the primary particles constituting the SPs. These remained unchanged before and after the catalytic reaction, demonstrating efficient coalescence prevention. Our findings underscore the importance of support pore size engineering for improving the stability of GaPt SCALMS catalysts and highlight, particularly, the high potential of using SPs in this context.

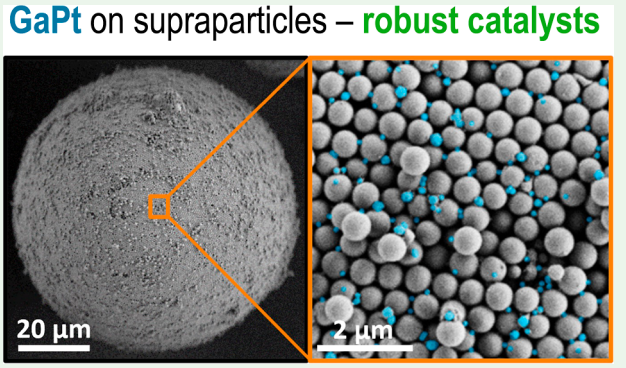

KEYWORDS: *SCALMS, gallium, liquid metal, catalysis, porous supports, supraparticles, propane dehydrogenation*

INTRODUCTION

Catalysis plays a crucial role in moving the chemical industry toward more sustainable ways of converting raw materials into valuable products. Among the relevant reactions, propane dehydrogenation (PDH) is an important intermediate step for the polymer industry as it provides propylene, which is the key base for polypropylene, a widely employed plastic in consumer products for health care, electronics, and home appliances.[1] The growing demand for propylene has led to a supply gap, necessitating advancements in PDH technologies to meet industrial needs.[2] Existing PDH processes predominantly rely on solid metal catalysts, but are plagued by inherent drawbacks, including sintering, carbon deposition, and catalyst deactivation over time.[3−8] These limitations underscore the need for novel catalyst materials that offer superior activity, selectivity, and stability.

Recently, supported catalytically active liquid metal solution (SCALMS) was introduced as a new concept to overcome these challenges.[9,10] SCALMS systems are composed of a porous support material, onto which a low-melting alloy is deposited. Prototype alloys are based on gallium and contain a small fraction of a catalytically active metal. Under reaction conditions, the supported alloy becomes liquid. The highly dynamic nature of the liquid metal has been shown to promote the formation of single atom active sites at the liquid metal-gas interface, where the reaction takes place due to the nonsolubility of the organic reactants in the liquid metal.[9,10] The specific nature of SCALMS promotes advantages such as efficient utilization of the active metal, high activity, enhanced selectivity, and suppressed coke formation.[10−13] In particular, the coke suppressing nature of SCALMS offers great advantages over commercially available heterogeneous PDH catalysts.[10−13] Consequently, in recent years, SCALMS have found applications across a wider spectrum of catalytic processes, including dehydrogenation and oligomerization reactions.[9−20]

Received: June 22, 2024
Revised: September 16, 2024
Accepted: September 19, 2024
Published: October 29, 2024

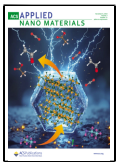

While coke suppression is a relevant advantage of SCALMS, distinct catalyst deactivation processes have been observed with these materials in PDH applications. These have been attributed to liquid metal droplet coalescence and phase separation[11,21,22] due to the high mobility of the liquid phase on the support.

Recently, we and others have shown that ultrasonication can be used for the straightforward and atom-efficient preparation of SCALMS.[15,23] This methodology builds on the ability of ultrasonication to break large metallic Ga nuggets dispersed in an appropriate solvent into nm-sized droplets with a broad droplet size distribution.[23] When deposited onto a typical support for heterogeneous catalysts, such as mesoporous SiO_2, their comparably large size prevents the droplets from infiltrating the pore network. Instead, they remain on the external surface of the support and form aggregates (Figure 1a).[10,15] Moreover, previous studies showed the influence of

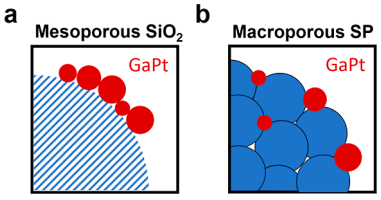

Figure 1. SCALMS on various support materials. Schematic illustration of GaPt SCALMS on a (a) commercial 10 nm SiO_2 support with high degree of aggregation and a (b) macroporous SP exhibiting an optimal pore structure for the separation and stabilization of individual GaPt droplets.

different supports on activity and a low tendency for cracking/coking.[11,20] Among the materials investigated, SiO_2-supported SCALMS showed inertness and least tendency for cracking/coking.[11] Nevertheless, deactivation was still observed with these improved support materials.[11,20,21] To suppress the main origins of deactivation (droplet coalescence and phase separation), the use of tailored support materials appears highly attractive, as a well-defined pore structure may prove suitable for immobilizing the liquid metal droplets under reaction conditions, as illustrated in Figure 1. A promising class of supports that provides pore systems with a high degree of tunability are supraparticles (SPs).

SPs are defined as typically spherical agglomerates of colloidal primary particles[24] and can be fabricated by the confined assembly of these primary particles in dispersion droplets, either by droplet-based microfluidics[25] with high uniformity or by scalable spray drying procedures.[26] The use of primary particles with uniform sizes provides SPs with a well-defined internal structure, which can impart additional functionality, such as structural coloration,[27−33] or enhanced powder flowability due to tailored surface roughness.[34]

Porosity is another important emergent property of SPs, which arises from the defined interstitial structure formed by the assembled primary particles.[35] These primary particles are bound by contact forces or solid bridges[36,37] and provide a fully interconnected, open porosity. This porosity can be tailored across multiple length scales,[32] spanning from small micro/mesopores[38] to large macropores created by sacrificial polymer primary particles.[39,40] This control of the internal pore structure makes such systems attractive for applications requiring percolated pore networks, including electrode design,[41] controlled release,[42,43] gas adsorption,[38] or catalysis.[20,44−47]

While conventional catalyst support design focuses on the creation of large surface areas created by the introduction of micro/mesopores,[46,47] the comparable large size of SCALMS catalyst particles necessitates control over the pore structure at larger dimensions, which are difficult to produce by conventional soft templating mechanisms.[48,49] The interstitial dimensions of SPs and the ability to add even larger pores by hard templating via sacrificial polymer particles[35,39,40] afford well-controlled macropore networks with >100 nm dimensions and are therefore ideal model systems to study catalyst performance and stability in SCALMS systems, as visualized in Figure 1b.

Here, we synthesize GaPt SCALMS on well-defined SP-based supports with controlled nanopore sizes to optimize the immobilization of the alloy droplets in the pore network and to prevent coalescence under reaction conditions. Furthermore, we investigate the influence of the support pore structure on the catalytic activity and stability in the PDH reaction at a temperature of 823 K. To this end, we prepare Ga droplets with diameters below 300 nm by using a top-down ultrasonication method. Subsequently, we fabricate SPs by spray drying of aqueous colloidal dispersions of silica primary particles and mixtures of silica and polystyrene (PS) primary particles. A wet impregnation step then immobilizes the Ga droplets on the SP supports, and the addition of a Pt precursor creates the active GaPt SCALMS materials by galvanic displacement.

EXPERIMENTAL SECTION

Materials. All chemicals were used as received. Gallium nuggets (size 3 mm, purity: 99.999%, Alpha Aesar), hexachloroplatinic acid (Pt bases: ≥37.5%, Sigma-Aldrich), propan-2-ol (purity ≥99.8%,

Table 1. Summary of Catalyst Performance of GaPt SCALMS Deposited on Different Supports in PDH[ab]

sample	support type	support pore size nm	GaPt droplet size distribution	X_0%	K_D h^{-1}	S_0%	P_0 $g_{propene}$ g_{Pt} h^{-1}
SiO_2-0 nm	silica	0	all sizes	2.5	0.046	98.3	4.7
SiO_2-10 nm	silica	10	all sizes	14.8	0.033	98.4	32.5
SiO_2-10 nm	silica	10	>300 nm	15.3	0.033	98.9	23.9
SiO_2-10 nm	silica	10	<300 nm	26.5	0.038	99.2	30.3
SP-45 nm	supraparticles	45	<300 nm	19.0	0.038	99.7	21.9
SP-100 nm	supraparticles	100	<300 nm	9.2	0.030	98.3	15.4
SP-200 nm	supraparticles	200	<300 nm	10.2	0.026	99.6	16.1
SP-320 nm	supraparticles	320	<300 nm	7.5	0.030	98.5	9.7

[a]Effects of GaPt droplet size and support pore size. [b]X_0 = initial conversion, S_0 = initial selectivity, K_D = deactivation rate normalized after 1 h TOS in PDH, and P_0 = initial productivity.

https://doi.org/10.1021/acsanm.4c03577
ACS Appl. Nano Mater. 2024, 7, 24356−24367

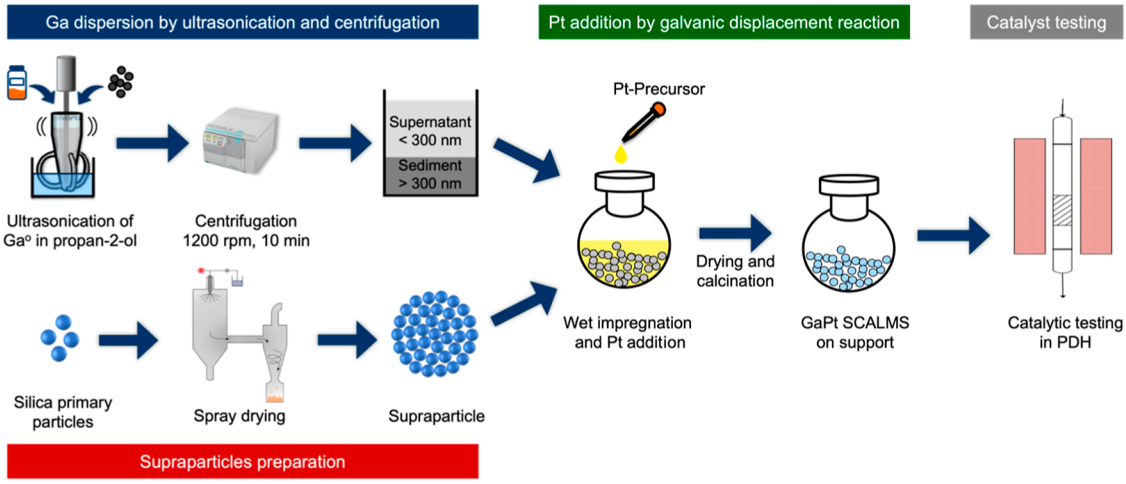

Figure 2. Preparation of GaPt SCALMS catalysts on SPs. Ga droplet dispersion with particle sizes <300 nm is prepared by ultrasonication and centrifugation. Simultaneously, the SPs are fabricated by spray drying of colloidal silica primary particles. Next, the Ga dispersion is deposited on the SP support, followed by the addition of catalytically active metal, Pt, by galvanic displacement. Finally, the obtained SCALMS systems are tested for PDH.

VWR chemicals), absolute ethanol (≥99.8%, NORMAPUR, VWR), ammonium hydroxide (25%, NORMAPUR, VWR), tetraethylorthosilicate (TEOS, ≥99%, GPR RECTAPUR, VWR), hydrochloric acid (HCl, 37%, VWR), acrylic acid (99%, Sigma-Aldrich), ammonium persulfate (≥98.0%, Sigma-Aldrich), sodium hydroxide (NaOH, ≥98%, Ph. Eur., USP, BP, in pellets), and aluminum oxide (90, neutral, Sigma-Aldrich) were all used as received. Styrene (≥99%, ReagentPlus, Sigma-Aldrich) was washed with 10 wt % aqueous NaOH solution and then passed through an aluminum oxide column to remove the inhibitor. It was then stored for no longer than 2 months at 8 °C before use. For water, a Purelab Flex 2 (Elga Veolia) purification unit was used (18.2 MΩ cm).

Synthesis of the GaPt SCALMS Catalyst. The GaPt SCALMS catalyst supported on SPs was prepared using the ultrasonication method, as described schematically in Figure 2.[11,15,19] Prior to the ultrasonication, the calculated amount of Ga nugget was premelted in an oven at 80 °C for 30 min. The premelting ensures the liquid state of gallium directly from the start of the sonication.[50] Once melted, gallium can remain in a super cooled liquid state at temperatures below the melting point for days.[12] After premelting, the ultrasonication was performed in 100 mL of propan-2-ol using 72% sonifier power for 30 min at a maximum temperature of 50 °C (Branson sonifier SFX 550 equipped with a microtip). The formed Ga droplet dispersion contains a broad droplet size distribution with sizes up to 1 μm, as reported in previous work.[11,15] To isolate Ga droplets of lower sizes (<300 nm), a centrifugation step was introduced. The entire Ga dispersion was centrifuged at 1200 rpm (225 rcf) for 10 min in a HERMLE Labortechnik centrifuge Z 366. The supernatant obtained after centrifugation contained Ga droplets with <300 nm size. This was confirmed by SEM image analysis. The residue was recycled to increase the yield of the desired size fraction maintaining the same particle size distribution, as shown in Figures S1 and S2.

Subsequently, the prepared GaNP dispersion with particle sizes <300 nm was physically deposited on the respective support by wet impregnation. The amount of the GaNP dispersion and the support used were calculated to achieve a 6 wt % loading of Ga on the support. After 5 min of stirring, the solvent was slowly removed using a rotary evaporator. Based on the Ga loading on the decorated support determined by inductively coupled plasma atomic emission spectroscopy (ICP-AES), the catalytically active metal, Pt, was introduced by galvanic displacement using a hexachloroplatinic acid precursor solution as described and calculated (see Supporting Information). The targeted Ga/Pt molar ratio was 45. This molar ratio describes a GaPt alloy with 2.2 atom % of Pt in Ga. From the phase diagram, this represents a GaPt alloy that is liquid under typical alkane dehydrogenation reaction conditions (773 K and above).[51] The final Ga and Pt loading of all of the catalysts prepared and tested in this work is summarized in Table S1.

Fabrication of Supraparticles. All SP samples were produced as reported in the literature.[35] First, colloidal silica primary particles were synthesized via the Stöber method.[52] Additionally, monodisperse PS primary particles were synthesized via surfactant-free emulsion polymerization.[53]

The SPs were prepared by spray drying of pure SiO_2 colloids and PS/SiO_2 colloid mixtures with a spray dryer (B290 mini, BÜCHI Labortechnik) under a nitrogen atmosphere. The colloid feed was atomized using a cocurrent flow two-fluid nozzle (Ø = 1.4 mm) at a gas flow of 357 L h^{-1} and feed flow of 3 mL min^{-1}. The aspirator flow was kept at 35 m^3 h^{-1}, and the inlet temperature was set to 130 °C. The prepared SPs were fractionated using sieves of mesh sizes 63 and 300 μm to separate larger SPs for catalytic testing and were subsequently calcined at 600 °C.

Characterization of Particle Size, Surface Morphology, Textural Properties, and Internal Structure. SPs and Ga droplets were imaged using SEM (Gemini 500, Zeiss) with an SE2 detector at an acceleration voltage of 1 kV and aperture size of 15 μm. Ga droplet sizes were measured via ImageJ software from the SEM images. To verify the particle sizes, additional TEM images using a Titan Themis3 300 (FEI) operated at 300 keV of Ga droplets before and after centrifugation were obtained in high-angle annular dark field (HAADF) scanning transmission electron microscopy (STEM) mode. Textural properties of the SPs were analyzed using Hg intrusion measurements by a PASCAL System (Thermo Scientific). The internal structure and Ga particle distribution within two types of SPs (320 and 45 nm pore size) were analyzed via nano X-ray computed tomography (nano-CT) using a Zeiss Xradia 810 Ultra lab-based X-ray microscope and by HAADF-STEM and energy-dispersive X-ray spectroscopy (EDXS) on FIB (focused ion beam) cross-sectional lamellae utilizing at Titan Themis^3 300 (FEI) operated at 300 kV acceleration voltage. FIB cross-section lamella preparation (Figure S3) was performed using a dual-beam FEI Helios NanoLab 660. Detailed information on the preparation and characterization procedure is available in the Supporting Information.

Characterization of Metal Loadings. The Ga and Pt loadings of the prepared reference and SCALMS catalysts were determined by ICP-AES using a Ciros CCD instrument (Spectro Analytical Instruments GmbH). The solid samples were digested with concentrated HCl/HNO_3/HF (attention: HF is a dangerous compound; relevant safety precautions must be taken) in a 3:1:1 volumetric ratio, using microwave heating to 493 K for 40 min. The instrument was calibrated for Pt (214.123 nm) and Ga (417.206 nm) with standard solutions of the elements before the analyses.

https://doi.org/10.1021/acsanm.4c03577
ACS Appl. Nano Mater. 2024, 7, 24356−24367

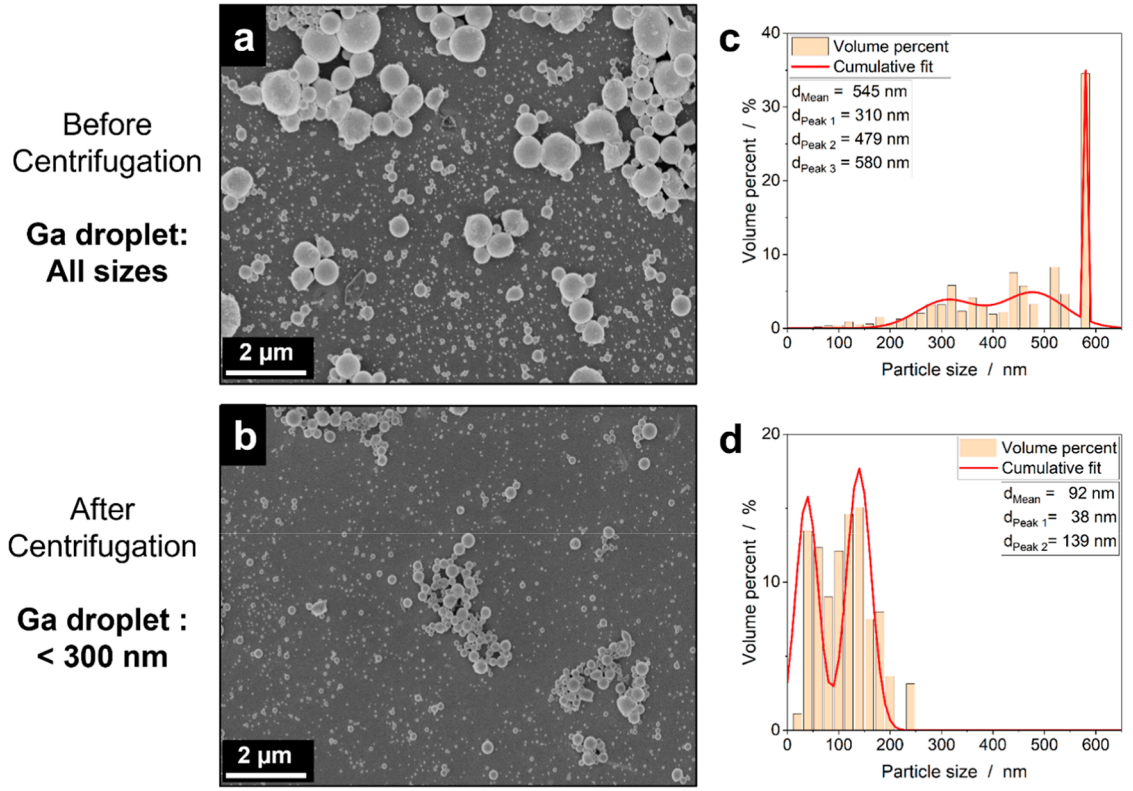

Figure 3. SEM analysis of Ga droplets produced by a combined ultrasonication/centrifugation procedure. (a) SEM image of the entire Ga droplet dispersion. (b) SEM image of Ga droplet dispersion after centrifugation at 1200 rpm for 10 min. (c) Volume-based particle distribution of the entire Ga droplet dispersion. (d) Volume-based distribution of Ga droplet dispersion centrifuged at 1200 rpm for 10 min. Process conditions: premelting of gallium, sonication time = 30 min, solvent = propan-2-ol (abs.), T_{max} = 35 °C, $C_{Ga,0}$ = 10 g L^{-1}, and energy input = 1.04 J s^{-1}.

Catalytic Testing—Propane Dehydrogenation in a Fixed Bed Reactor. To test the catalytic performance of the prepared catalysts in PDH, 1.5 g of each catalyst was loaded in a fixed bed quartz tubular reactor (Figure S4). The reactor was heated to set points of 823 K and 0.12 MPa at 10 K min^{-1} under an inert atmosphere of 100 mL_N min^{-1} argon (99.998% purity, Air Liquide). Prior to the start of PDH, the catalyst was pretreated under the reductive atmosphere of 19.5 mL_N min^{-1} hydrogen (99.999% purity, Air Liquide) diluted with 80.5 mL_N min^{-1} argon for 3 h at 823 K. After the H_2 pretreatment, a purge stream of 100 mL_N min^{-1} of argon was sent for 60 min to remove any residual H_2. The reaction was started by supplying 8.9 mL_N min^{-1} propane (99.95% purity, Air Liquide) as the feed gas diluted with 90.4 mL_N min^{-1} argon. The gas hourly space velocity (GHSV) was set at 3950 mL_{gas} $g_{Cat.bed}^{-1}$ h^{-1} under the reaction conditions. The gases were dosed by mass flow controllers (MFC, Bronckhorst). All parts exposed to reagents, except for the fixed bed quartz reactor, were made of stainless-steel type 1.4571. A tubular split furnace heated the quartz glass fixed bed reactor. All reactor tubes and pipes outside the furnace were held at 373 K by using heating tapes and fiberglass tape insolation.

Product Analysis Using Online Gas Chromatography. The product gas mixture was analyzed using online gas chromatography (GC) on a Bruker 456 GC equipped with a GC-GASPRO column (30 m × 0.320 mm) having a thermal conductivity detector for detecting the light compounds (H_2, Ar, and He) and a flame ionization detector for detecting the C1−C3 hydrocarbons. The sample time for peak identification and resolving was 10 min. The peak area obtained from the GC data and the calibration factors were used in calculating the mole fraction (x) of each compound. The conversion for propane ($X_{propane}$), the selectivity for the desired product propene ($S_{propene}$), deactivation rate (K_d), which describes the stability of the catalyst, and the catalyst productivity (productivity) were calculated using the equations below

$$\text{conversion}_{propane} = \frac{x_{propane,in} - x_{propane,out}}{x_{propane,in}} \quad \text{(S1)}$$

$$\text{selectivity}_{propene} = \frac{x_{propene}}{x_{propene} + x_{methane} + x_{ethane} + x_{ethene}} \quad \text{(S2)}$$

$$\text{deactivation rate } K_d = \frac{\Delta X_{propane}}{\Delta TOS \cdot X_{1hTOS}} \quad \text{(S3)}$$

$$\text{productivity} = \frac{\dot{n}_{propane,in} \cdot S_{propene} \cdot X_{propane} \cdot MW_{propene}}{m_{pt}} \quad \text{(S4)}$$

where x_i is the mole fraction of the respective compound i calculated based on the GC analysis and $\Delta X_{propane}$ and ΔTOS represent the net change in conversion and time between 1 and 15 h time-on-stream (TOS), respectively. $\dot{n}_{propane,in}$ represents the mole flow rate of propane in the feed, $MW_{propene}$ is the molar weight of propene, while m_{pt} represents the mass of Pt in the catalyst bed.

RESULTS AND DISCUSSION

The GaPt SCALMS catalyst was prepared using the well-established ultrasonication method as previously reported by some of us.[11,15,19] This involves the breakdown of large metallic Ga nuggets into nanosized droplets which are then deposited onto a porous support.[23] While this procedure offers some practical advantages (simplicity of operation and high atom-efficiency) against the previously reported organo-chemical approach,[9−11] it leads to the formation of Ga droplets with a broad droplet size distribution ranging from 0.05 to 1 μm. These droplet sizes are much larger than those of conventional solid catalyst nanoparticles and prevent the

https://doi.org/10.1021/acsanm.4c03577
ACS Appl. Nano Mater. 2024, 7, 24356−24367

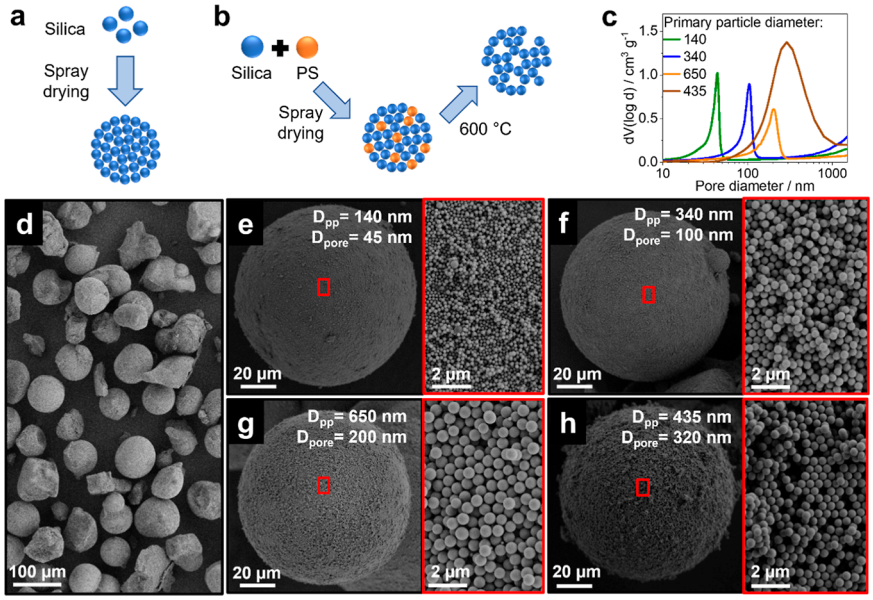

Figure 4. Spray-dried nanoporous SPs. (a) Schematic illustration of SP fabrication using silica colloids. (b) Schematic illustration of templated SP fabrication using a mixture of silica and sacrificial PS to introduce large, templated pores. (c) Pore size distributions of the prepared SPs measured via mercury porosimetry reveal an increase in average pore size with increasing primary particle diameter. (d) Overview SEM image of a typical spray-dried SP powder batch. (e–g) SEM analysis of the fabricated SPs featuring (e) primary particle diameter (D_{pp}) of 140 and 45 nm pore diameter (D_{pore}), (f) D_{pp} of 340 and 100 nm D_{pore}, and (g) D_{pp} of 650 and 200 nm D_{pore}. Insets depict the increase in diameter of the constituent primary particles and the resulting increase in pore size. (h) SEM analysis of templated SP featuring a D_{pp} of 435 and 320 nm D_{pore}. Notably, large, templated pores resulting from the removal of PS particles used as hard templated can be observed in the inset. Process conditions (spray drying): drying gas flow = 357 mL min^{-1}, feed flow = 3 mL min^{-1}, aspirator flow = 35 mL min^{-1}, inlet temperature = 130 °C, and calcination temperature = 600 °C.

efficient infiltration of such droplets into technical mesoporous support materials like SiO_2. Figure 2 shows the concept of preparing defined Ga droplets and the preparation of SPs to enable efficient integration of the formed droplets into the SP support. This is achieved using a 2-fold approach. First, the average size of the Ga droplets needs to be reduced. Second, supports with larger porosity need to be developed.

To achieve the first aim, the formed Ga dispersion after ultrasonication was centrifuged at 1200 rpm for 10 min to selectively sediment undesirable large Ga droplets. Figure 3 shows the SEM images and volume distributions of the Ga droplets before and after centrifugation. The ultrasonication produced Ga droplets with a mean diameter of 545 nm (Figure 3a,c), which was reduced to 92 nm after the centrifugation step (Figure 3b,d). After centrifugation, the largest droplet measured was no more than 240 nm, as determined from the volumetric distribution calculated from SEM images (see Figure S5 for additional images). These findings were further supported by HAADF-STEM measurements performed on ultrasonicated Ga droplets without and with the additional centrifugation step (Figure S5). Importantly, the unwanted fraction of larger droplets can be recycled back into the fabrication process and ultrasonicated again to continuously increase the yield of the desired Ga droplet size fraction <300 nm, ensuring an efficient use of all Ga (Figure S2).

To provide tailored support materials with the required larger porosity enabling the infiltration of the prepared Ga droplets, we fabricate SPs with controlled average pore sizes. Initially, we synthesize colloidal silica using the Stöber process,[54] yielding dispersions of primary particles with average sizes ranging from 140 to 650 nm and a narrow size distribution. These primary particles are then consolidated into SPs via spray drying (Figure 4a), resulting in well-defined SPs devoid of any irregularities (such as hollowness or buckling) often associated with rapid drying processes (Figures 4d and S6).[55−57] By varying the size of the primary particles during spray drying, we tailor the size of the interstitial pores, with larger primary particles yielding SPs with larger average pore sizes.[35] Using this method, SP supports with pore sizes of 45 (from 140 nm primary particles), 100 (from 340 nm primary particles), and 200 (from 650 nm primary particles) are prepared. We confirm these pore characteristics through mercury porosimetry measurements, which show narrow pore size distribution curves indicative of a uniform pore system inside the SPs (Figure 4c). By virtue of the uniform primary particles, the consolidated SPs also exhibit a defined surface roughness composed of primary particles in contact with the surface. The roughness features thus scale directly with the size of the constituent primary particles.[58] Both the change in pore size and the defined surface roughness are evident in representative SEM images, where the relative change in interprimary particle distance and the ordered surface structure is readily observed (Figure 4e–g).

To ensure effective immobilization of the Ga droplet population (<300 nm GaPt droplet, Figure 3d) onto the SP-based support materials, we extend the pore size to values larger than 300 nm. To this end, we take advantage of a hard templating approach[35,39,40] and incorporate PS colloidal particles in predefined size and volume ratios to fabricate composite SPs. The silica colloidal particles form the SP structure, while the PS particles are removed after consolidation via calcination (T = 600 °C) (Figure 4b). The number of templated pores scales directly with the amount of PS in the initial composition of the SPs and inversely with their mechanical strength.[35,40] Therefore, to maintain a balance between the two properties, we use 30 vol % PS in the initial

https://doi.org/10.1021/acsanm.4c03577
ACS Appl. Nano Mater. 2024, 7, 24356−24367

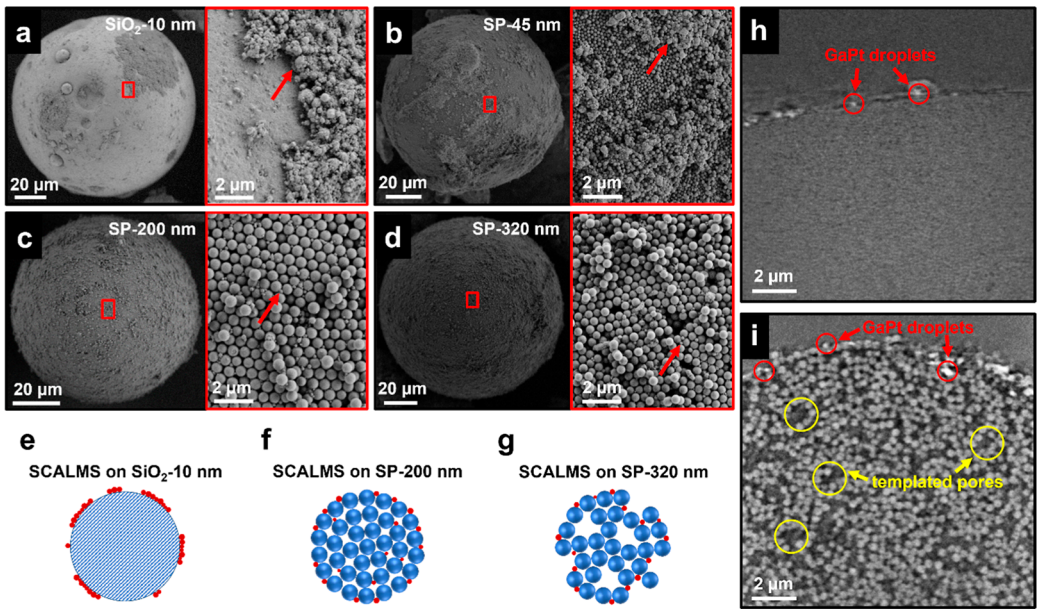

Figure 5. Immobilization of Ga droplets on commercial and tailored nanoporous SP-based supports. (a) SEM analysis of a commercial silica support (Supelco; 10 nm average pore size) after immobilization of Ga. The inset shows large agglomerates on the surface due to the insufficiently small pore size. (b–d) SEM analysis of the Ga immobilized on SP supports of pore size 45, 200, and 320 nm, respectively. Notably, agglomeration of gallium droplets on 45 nm SPs is evident in the inset. In contrast, on 200 and 320 nm SPs, gallium droplets exhibit a homogeneous distribution across the surface without visible agglomeration. Red arrows indicate the location of Ga droplets. (e–g) Schematic illustrations of the prepared SCALMS on 10 nm commercial, 200 nm SP, and 320 nm SP, respectively. (h,i) High-resolution nano-CT reconstructed slices of the SP-45 nm and SP-320 nm sample, respectively, revealing that only the SP-320 nm sample exhibits a penetration of Ga droplets into the outer rim of the porous templated SP structure down to a depth of ∼1.5 μm. However, deeper inside both SP samples, no larger Ga droplets (>50 nm, bright contrast in the reconstructed slices and dark in the projected images) are detected (cf. Figure S7 and Videos S1,S2,S3, and S4).

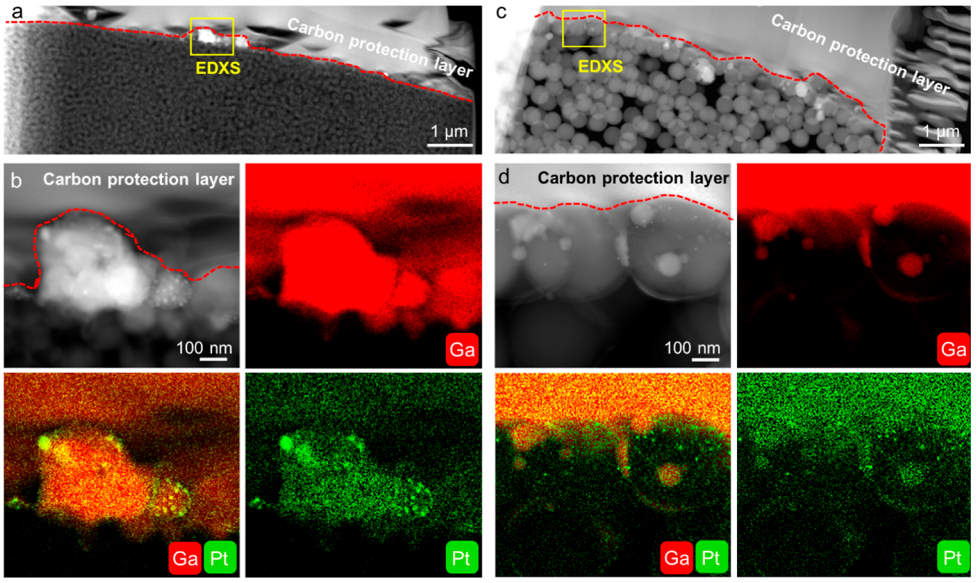

Figure 6. Elemental distribution of Ga and Pt in the SP surface region for SP-45 nm and SP-320 nm samples. HAADF-STEM cross-section images showing the surface of the SPs with pore sizes of (a) 45 and (c) 320 nm. HAADF-STEM images and the corresponding EDXS elemental maps for the SPs with pore sizes of (b) 45 and (d) 320 nm.

colloid mixture while using equal size ratios to achieve a homogeneous distribution of the templated pores.[34]

The representative SEM images of the templated SPs showcase the ordered surface structure and the large templated macropores resulting from the removal of the PS particles from the surface of the SPs (Figure 4h inset). The pore size distribution exhibits a shift to larger values than expected for the constituent primary particle sizes due to the presence of large, templated pores (Figure 4c).[35] Additionally, besides the spherical pores left by individual PS particles, the relatively large number of PS particles in the colloid mixture lead to assembly structures with multiple PS particles in direct contact, resulting in large, nonspherical pores upon calcination.[35] These templated pores, combined with interstitial pores arising from the assembly of remaining silica particles, translate into an increase in the width of the pore size distribution.

https://doi.org/10.1021/acsanm.4c03577
ACS Appl. Nano Mater. 2024, 7, 24356−24367

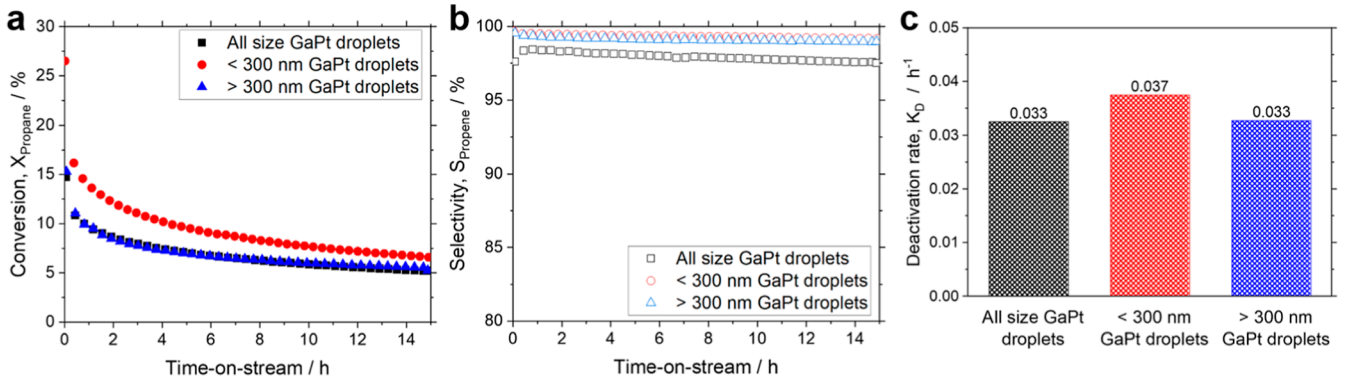

Figure 7. Catalytic performance of GaPt SCALMS on commercial SiO_2 supports in PDH. (a) Effect of GaPt droplet size on conversion (filled symbols), (b) selectivity (open symbols), and (c) deactivation rate after 15 h TOS in PDH (bar chart). All size GaPt droplets (black), <300 nm GaPt droplets (red), and >300 nm GaPt droplets (blue). Catalyst bed: 1.5 g catalyst; H_2 pretreatment conditions: H_2 19.5 mL_N min^{-1}, Ar flow 80.5 mL_N min^{-1}, 823 K, and 0.12 MPa; PDH reaction conditions: C_3H_8 flow 8.9 mL_N min^{-1}, Ar flow 90.4 mL_N min^{-1}, 823 K, 0.12 MPa, and GHSV 3950 mL_{gas} $g_{Cat.bed}^{-1}$ h^{-1}.

Next, we immobilized Ga droplets onto the SPs through wet impregnation. Here, SPs are introduced into a dispersion of Ga droplets in isopropanol, and the solvent is gradually evaporated using a rotary evaporator, as described in Figure 2. As the solvent evaporates, capillary forces drive the Ga droplets onto the SPs, effectively immobilizing them. Upon complete drying, SEM analysis of a commercial reference support material with an average pore size of 10 nm reveals that all the Ga droplets sit on the surface, forming large aggregates (Figure 5a,e). Clearly, the larger size of the Ga droplets cannot enter the pore system, nor are they efficiently trapped as individual particles at the surface. Similarly, the SEM images for SP-45 nm (Figure 5b) also show large agglomerates of Ga droplets on the surface, underlining the inadequacy of small pore sizes for immobilization.

In contrast, SPs with a larger pore size of 200 nm show individual Ga droplets uniformly distributed across the surface and typically trapped in interstitial sites between primary particles (Figure 5c,f). Remarkably, we observe minimal agglomeration as the droplets are now separated by the primary particles. Further increasing the pore size to 320 nm via templating yields a similar homogeneous distribution of Ga droplets on the surface (Figure 5d,g). Furthermore, the analysis of reconstructed cross-sectional nano-CT slices of the SP-45 nm (Figure 5h) and SP-320 nm (Figures 5i and S7 and Videos S1,S2,S3 and S4) samples reveals the presence of Ga droplets deeper (~1.5 μm) inside the templated SP structure for the SP-320 nm sample. We attribute this to the large, templated pores present on the surface that facilitate deeper penetration of Ga droplets into the SP. Consequently, a larger portion of the pore system is now available for Ga droplet immobilization. In general, it is evident that the combination of a larger pore size and templated pore structures leads to reduced agglomeration and, therefore, a more homogeneous distribution of Ga on the support material.

Following the immobilization of Ga, the active metal Pt was introduced into the droplets by galvanic displacement using the Pt precursor hexachloroplatinic acid (see Suppoting Information for more details) to form the final catalytically active GaPt alloy, maintaining a consistent Ga/Pt ratio across all prepared samples (Table S1). Moreover, we performed more detailed analyses at higher resolution using HAADF-STEM imaging and STEM-EDXS on FIB cross-sectional lamellae, as shown in Figure 6 (see Figure S3 for lamellae preparation). These investigations confirm that at the surface of both SP-45 nm and SP-320 nm samples, larger Ga-rich droplets with sizes up to a few hundred nanometers were deposited on the surface features of the SPs, with their surfaces covered by small Pt particles. To reveal the depth-dependent Ga and Pt particle distribution and density within the SPs, an investigation of the internal structure of the SPs was performed (Figure S8). Notably, Pt particles were found to be distributed throughout the SPs, with significantly higher Pt density observed in SPs with 320 nm pores compared with those with 45 nm pores. Only in the SP-320 nm sample, due to the larger pore size, we observe (both in nano-CT reconstructed slices and FIB cross-sectional cuts) silica spheres wetted with Ga-rich material down to a depth of a few microns (see Figures S7 and S9). In this region, almost no single Pt NPs are observed on the primary silica particles (Figure S9a). However, deeper inside the SP, a homogeneous distribution of single Pt NPs is discovered (Figure S8b,c). The Pt depletion in the outer few μm of the SP is not observed for the SP-45 nm sample.

Prior to discussing the effect of support pore size on the catalytic performance of SCALMS, we investigated the influence of the GaPt droplet size on the catalytic performance of GaPt SCALMS in PDH. For this, catalysts with different GaPt droplet size were prepared and deposited on a mesoporous spherical silica support with a pore size of 10 nm. We compare the catalytic performance of <300 nm GaPt droplets (as selectively obtained by the introduction of a centrifugation step after ultrasonication) with >300 nm GaPt droplets, both deposited on a commercial mesoporous silica support. For reference, a catalyst consisting of GaPt droplets of all sizes was also prepared on the same support. To confirm the absence of blank activity, a bare SiO_2-10 nm support was tested under identical PDH conditions (Figure S10). Figure 7 shows the effect of the alloy droplet size on the conversion, selectivity, and deactivation rate in PDH over 15 h TOS. The catalyst prepared using <300 nm GaPt droplets showed the best performance with an initial conversion of 26.5%, while the catalyst prepared using >300 nm GaPt droplets showed only an initial conversion of 15.3%. Interestingly, the activity profile of the material produced using >300 nm GaPt droplets overlaps largely with the reference material prepared using the whole droplet size distribution. We attribute the higher initial conversion with <300 nm GaPt droplets to the larger available

https://doi.org/10.1021/acsanm.4c03577
ACS Appl. Nano Mater. 2024, 7, 24356−24367

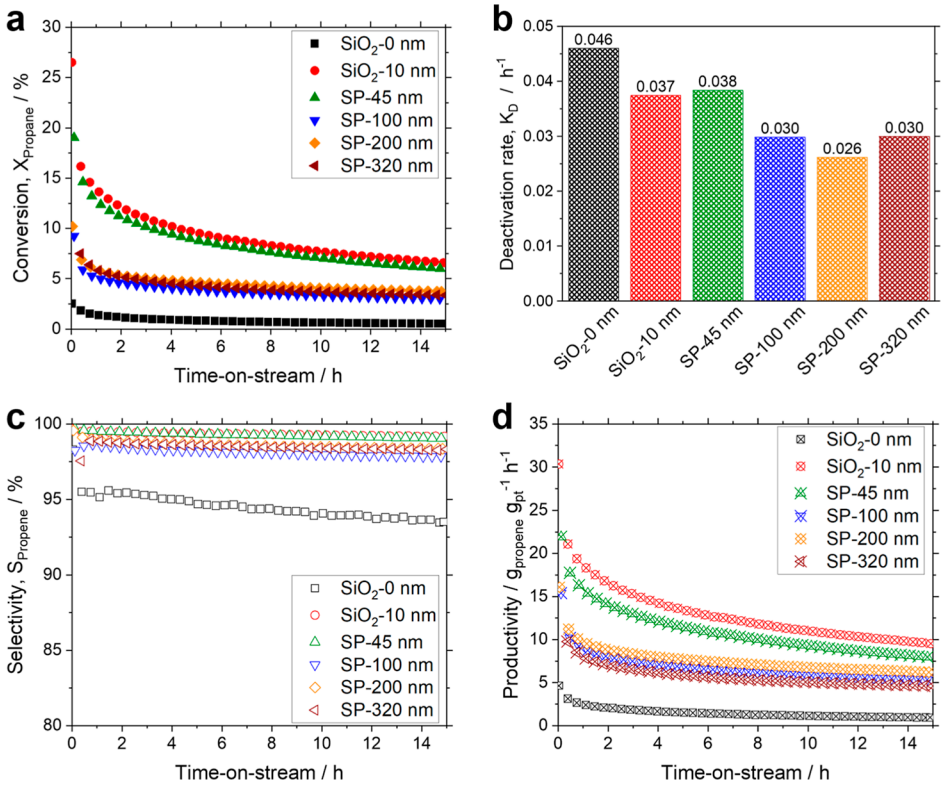

Figure 8. Effect of support pore size on the catalytic performance of GaPt SCALMS supported on silica SPs in PDH. (a) Effect of support pore size on conversion (filled symbols), (b) deactivation rate normalized between 1 and 15 h TOS in PDH (bar chart), (c) selectivity (open symbols), and (d) productivity over 15 h TOS (crossed symbols). SiO_2-0 nm (black), SiO_2-10 nm (red), SP: 45 nm (green), SP-100 nm (blue), SP-200 nm (orange), and SP-320 nm (brown). Catalyst bed: 1.5 g catalyst; H_2 pretreatment conditions: H_2 19.5 mL_N min^{-1}, Ar flow 80.5 mL_N min^{-1}, 823 K, and 0.12 MPa; PDH reaction conditions: C_3H_8 flow 8.9 mL_N min^{-1}, Ar flow 90.4 mL_N min^{-1}, 823 K, 0.12 MPa, and GHSV 3950 mL_{gas} $g_{Cat.bed}^{-1}$ h^{-1}. The highest initial productivity is observed for SiO_2-10 nm and SP-45 nm with initial productivity values of 30.4 $g_{propene}$ g_{Pt} h^{-1} and 21.9 $g_{propene}$ g_{Pt} h^{-1}, respectively. This is followed by a pronounced deactivation leading to final productivity values of 9.5 $g_{propene}$ g_{Pt} h^{-1} and 7.9 $g_{propene}$ g_{Pt} h^{-1} after 15 h TOS. The SPs with larger pore sizes SP-100 nm and SP-200 nm show similar initial productivities of 15.4 $g_{propene}$ g_{Pt} h^{-1} and 16.1 $g_{propene}$ g_{Pt} h^{-1}, respectively, while the catalyst on SP-320 nm shows lower initial productivity of 9.8 $g_{propene}$ g_{Pt} h^{-1}. Similarly, the larger pore size SPs of SP-100 nm, SP-200 nm, and SP-320 nm display final productivity values of 4.6−6.2 $g_{propene}$ g_{Pt} h^{-1}. The nonporous support SiO_2-0 nm shows a very low final productivity of only 1.0 $g_{propene}$ g_{Pt} h^{-1}. Table 1 summarizes the key performance data for all SCALMS materials discussed in this work.

metal-gas interface in the sample prepared using the smaller droplet sizes. Aside from a marginally lower selectivity (98%) for the "all size" Ga droplet sample, the particle size did not seemingly affect the selectivity (Figure 7b). The high and constant selectivity above 98% for over 15 h TOS highlights the attractive catalytic performance of all SCALMS systems investigated in this study. The catalyst productivity, which normalizes the activity of the catalyst per gram of active metal, is summarized in Figure S11. All SCALMS materials displayed in Figure 7 show a pronounced exponential loss in activity over the 15 h TOS. In fact, the initial high activity obtained using the smaller GaPt droplet size fraction (<300 nm) is lost over time as all tested materials approached similar conversion values of 5.5% and 6.5% after 15 h TOS. The reason for this exponential loss in activity has been ascribed to the mobility-induced coalescence of the GaPt droplet.[21] In all cases displayed in Figure 7, the GaPt droplets sit on the external surface of the support, which has a small pore size of 10 nm. As a result, droplet coalescence results in stronger deactivation rates (0.037 h^{-1} for the <300 nm GaPt droplets; 0.033 h^{-1} for both the >300 nm GaPt droplets and all size GaPt droplets), as shown in Figure 7c. Note that deactivation by coking as major driving force for loss of activity in SiO_2-based GaPt SCALMS catalyst can be excluded as reported in the literature.[11]

Having established the performance of various GaPt droplet size fractions and the significant deactivation using commercial supports, we now investigate the effect of support pore sizes on the catalytic performance. To this end, we use the nanoporous SP support and immobilize <300 nm GaPt droplets onto them, as shown in Figure 5. As a reference, we employ <300 nm GaPt droplets deposited on a nonporous silica support (SiO_2-0 nm) and the 10 nm commercial silica support (SiO_2-10 nm) used to evaluate the catalytic performance of the different droplet size fractions (shown in Figure 7). Figure 8 summarizes the effect of the support pore size on the conversion, deactivation rate, selectivity, and productivity of GaPt SCALMS in PDH. An exponential drop in conversion within the first hour of TOS is observed for all catalysts, as shown in Figure 8a. In this comparison, the reference catalyst SiO_2-10 nm achieved the highest initial conversion of 26.5%. Despite a lower initial conversion of 19.0% using SP-45 nm, the catalyst followed a similar activity profile as SiO_2-10 nm over the 15 h reaction time investigated. This led to final conversion values of 6.0% and 6.5% for the SP-45 nm and the reference SiO_2-10 nm material, respectively.

The SEM images shown in Figure 5a,b and the nano-CT reconstruction in Figure 5h reveal that due to the small pores in SiO_2-10 nm and SP-45 nm, most of the <300 nm GaPt

https://doi.org/10.1021/acsanm.4c03577
ACS Appl. Nano Mater. 2024, 7, 24356−24367

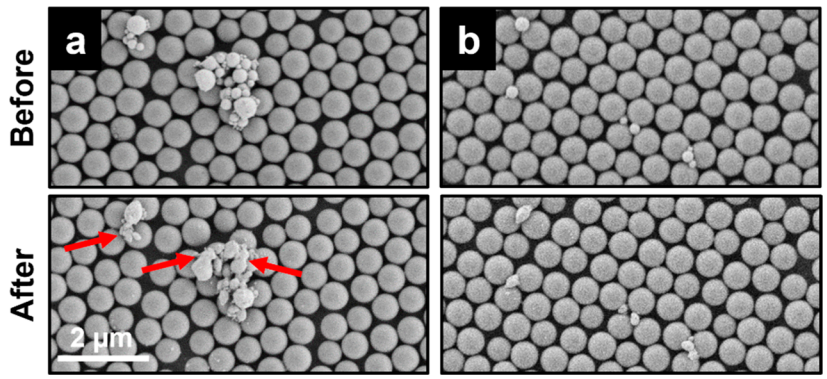

Figure 9. Identical location SEM analysis of GaPt droplets immobilized on a single layer of silica primary particles, mimicking the situation in impregnated SPs before and after exposure to reaction conditions. (a) Agglomerated droplets underwent coalescence after exposure to reaction conditions (red arrows indicate the coalesced droplets), (b) whereas individual droplets trapped in the interstitial sites of the colloidal monolayer remained immobilized. Note, however, that the droplets deformed after the reaction.

droplets are located on the surface of the support in the form of large agglomerates. In both cases, the <300 nm GaPt droplets are not immobilized on the support and, as a result, show higher initial activity due to their easier accessibility but are prone to deactivation caused by mobility-induced coalescence. Noteworthy, the catalysts deposited on the SPs with larger pore sizes (SP-100 nm, SP-200 nm, and SP-320 nm) show a completely different activity profile. Despite the lower initial conversion of 9.2%, 10.2%, and 7.5%, respectively, the larger pore-sized SPs show significantly improved stability over the 15 h reaction time investigated. The low conversion obtained with the larger pore-sized SPs is presumable due to loss of Pt into the bulk of the support (see Figure S8 TEM cross-sectional lamella showing Pt density in the bulk of the support). The improved stability of these samples, however, is certainly not due to the low conversion, as we confirm with a reference experiment performed using a nonporous silica, SiO_2-0 nm support, which showed an initial conversion of 2.5% and a final conversion of 0.5% after 15 h reaction time. This nonporous sample shows a deactivation rate of 0.046 h^{-1} over the same reaction time. The commercial support (SiO_2-10 nm) and SP-45 nm exhibit a deactivation rate of 0.038 h^{-1}. In comparison, the SPs with SP-100 nm, SP-200 nm, and SP-320 nm show improved catalyst stability, evidenced by lower deactivation rates down to 0.030 h^{-1} for the SP-320 and down to 0.026 h^{-1} for the SP-200-supported material (see Figure 8b). We suggest that this stabilization effect is caused by the immobilization of the droplets in the porous network of the SP that prevents further coalescence. TEM cross-section and nano-CT analysis, described in Figures 5 and 6, show that the GaPt droplets penetrate the SP-320 nm (a few μm), corroborating this interpretation. All the catalysts on the different supports tested in this work showed selectivities for the desired product propene above 98% over 15 h TOS, except with SiO_2-0 nm, which reached only 95% selectivity and showed the strongest cracking tendencies (Figure 8c). The catalyst productivity (Figure 8d), which normalizes the activity of the catalyst per gram of active metal, shows trends similar to those observed with conversion.

We attribute the difference in catalyst stability to the different pore structures. In SiO_2-10 nm and SP-45 nm, the GaPt droplets exist agglomerated exclusively on the support surface (Figure 5a,b). In contrast, the SP support SP-100 nm to SP-320 nm shows trapping of GaPt droplets in the surface roughness features and increasing penetration into surface-near pores (Figure 5c,d). These results are further corroborated by TEM cross-section and nano-CT analyses performed on the SP-320 nm sample, which showed a penetration of GaPt alloy, either as droplets or wetted layer, into the surface-near first few μm (Figures 5i and S7). This trapping of individual GaPt droplets affords an efficient immobilization, as a direct contact between individual particles is minimized. This immobilization of the GaPt droplets impedes the temperature-induced mobility and, as a result, suppresses the coalescence of the droplets during the reaction that is in part responsible for the strong deactivation observed in the nonporous and the smaller pore size supports. Interestingly, individual Pt NPs can be found inside both SP-45 nm and SP-320 nm samples with constant NP density, respectively (except for this surface-near region in SP-320 nm where the alloy droplets were seen). These individual Pt NPs arise due to the synthesis method of adding Pt by wet impregnation. In general, the overall Pt NP density was higher for the SP-320 nm sample compared with SP-45 nm (Figure S8). We note, however, that reference Pt NP deposited on SPs did not show activity for PDH under the same conditions investigated in this work (Figure S12), indicating the importance of the dynamic single atom characteristics within the liquid SCALMS system for the observed catalytic reaction.

To further investigate the state of the GaPt droplets and the immobilizing effect of the support structure after the reaction, we use identical location SEM technique[22,59,60] to analyze GaPt droplets deposited on a single layer of silica primary particles (650 nm), which provides a surface roughness that is identical to the SP support with 200 nm pores. We image the exact same area with deposited GaPt droplets before and after the catalytic PDH reaction. As can be seen in Figure 9a, an area that showed agglomerates of many small GaPt droplets before PDH changes significantly after the reaction and coalescence effects of particles in direct contact can be observed. This points toward the proposed mobility of the smaller droplets under reaction conditions, which can merge into larger droplets. In contrast, isolated GaPt droplets that are immobilized at the interstitial sites of the colloidal monolayer, shown in Figure 9b, did not show any signs of coalescence and remained trapped as individual particles within the colloidal layer of colloidal particles. Noteworthy, a change in the shape of these individual droplets is observed, indicating that they indeed liquefied at reaction conditions, where the solid Ga_2O_3

https://doi.org/10.1021/acsanm.4c03577
ACS Appl. Nano Mater. 2024, 7, 24356−24367

skin is seemingly removed in the presence of Pt under reductive reaction conditions.

CONCLUSIONS

In this study, we systematically elucidate how the pore size and surface structure of a support material affect the state of GaPt droplets and the stability of the SCALMS catalysis. We find that a stable SCALMS system, characterized by low deactivation rates, arises if the pore structure of the support is matched to the size distribution of the active liquid metal droplets in a way that individual liquid metal droplets are efficiently immobilized at the surface and near-surface pores of the support. In our case, GaPt droplets on SP-based supports showed a successful immobilization with pore sizes > ∼100 nm, while smaller pore sizes produced agglomerated GaPt structures on top of the SP surface. The successful immobilization of these GaPt droplets within the SP pore network was validated by nano-CT and identical location SEM. This was further correlated with a decreased deactivation rate compared to both commercial references and SPs with smaller pores. Our study showcases the importance of support development to harvest the potential of SCALMS systems, where the size of the catalyst particles and their liquid nature warrant distinct characteristics of the support material to enable stable catalytic performance.

ASSOCIATED CONTENT

Data Availability Statement

The data that support the findings of this study are available in the Supporting Information of this article.

Supporting Information

The Supporting Information is available free of charge at https://pubs.acs.org/doi/10.1021/acsanm.4c03577.

Material synthesis, cross-sectional TEM, and nano-CT characterization of the catalyst on different supraparticle supports; SEM characterization of Ga droplets and supraparticles; flow scheme of the reactor; and conversion and selectivity graphs of reactor blank activity and reference materials (PDF)

Reconstructed slices of the nano-CT HRES PC tilt series of <300 nm GaPt droplets on SP-45 nm (MP4)

Tilt series of the nano-CT HRES PC measurement of <300 nm GaPt droplets on SP-45 nm (MP4)

Reconstructed slices of the nano-CT HRES PC tilt series of <300 nm GaPt droplets on SP-320 nm (MP4)

Tilt series of the nano-CT HRES PC measurement of <300 nm GaPt droplets on SP-320 nm (MP4)

AUTHOR INFORMATION

Corresponding Authors

Marco Haumann − *Friedrich-Alexander-Universität Erlangen-Nürnberg (FAU), 91058 Erlangen, Germany; Department of Chemistry, Research Centre for Synthesis and Catalysis, University of Johannesburg, Johannesburg 2092, South Africa*; orcid.org/0000-0002-3896-365X; Email: marco.haumann@fau.de

Nicolas Vogel − *Friedrich-Alexander-Universität Erlangen-Nürnberg (FAU), Institute of Particle Technology, 91058 Erlangen, Germany*; orcid.org/0000-0002-9831-6905; Email: nicolas.vogel@fau.de

Peter Wasserscheid − *Friedrich-Alexander-Universität Erlangen-Nürnberg (FAU), 91058 Erlangen, Germany; Forschungszentrum Jülich GmbH, Helmholtz-Institute Erlangen-Nürnberg for Renewable Energy (IEK-11), 91058 Erlangen, Germany; Forschungszentrum Jülich GmbH, Institute for a Sustainable Hydrogen Economy (INW), 52428 Jülich, Germany*; Email: peter.wasserscheid@fau.de

Authors

Nnamdi Madubuko − *Friedrich-Alexander-Universität Erlangen-Nürnberg (FAU), 91058 Erlangen, Germany*

Umair Sultan − *Friedrich-Alexander-Universität Erlangen-Nürnberg (FAU), 91058 Erlangen, Germany; Friedrich-Alexander-Universität Erlangen-Nürnberg (FAU), Institute of Particle Technology, 91058 Erlangen, Germany*; orcid.org/0000-0003-3765-1061

Simon Carl − *Institute of Micro- and Nanostructure Research (IMN) & Center for Nanoanalysis and Electron Microscopy (CENEM), Friedrich-Alexander-Universität Erlangen-Nürnberg (FAU), 91058 Erlangen, Germany*

Daniel Lehmann − *Friedrich-Alexander-Universität Erlangen-Nürnberg (FAU), 91058 Erlangen, Germany*

Xin Zhou − *Institute of Micro- and Nanostructure Research (IMN) & Center for Nanoanalysis and Electron Microscopy (CENEM), Friedrich-Alexander-Universität Erlangen-Nürnberg (FAU), 91058 Erlangen, Germany*; orcid.org/0000-0002-4250-2768

Alexander Soegaard − *Friedrich-Alexander-Universität Erlangen-Nürnberg (FAU), 91058 Erlangen, Germany*

Nicola Taccardi − *Friedrich-Alexander-Universität Erlangen-Nürnberg (FAU), 91058 Erlangen, Germany*

Benjamin Apeleo Zubiri − *Institute of Micro- and Nanostructure Research (IMN) & Center for Nanoanalysis and Electron Microscopy (CENEM), Friedrich-Alexander-Universität Erlangen-Nürnberg (FAU), 91058 Erlangen, Germany*; orcid.org/0000-0003-0498-7271

Susanne Wintzheimer − *Department of Chemistry and Pharmacy, Inorganic Chemistry, Friedrich-Alexander-Universität Erlangen-Nürnberg (FAU), 91058 Erlangen, Germany; Fraunhofer-Institute for Silicate Research ISC, 97082 Würzburg, Germany*; orcid.org/0000-0003-3791-8117

Erdmann Spiecker − *Institute of Micro- and Nanostructure Research (IMN) & Center for Nanoanalysis and Electron Microscopy (CENEM), Friedrich-Alexander-Universität Erlangen-Nürnberg (FAU), 91058 Erlangen, Germany*; orcid.org/0000-0002-2723-5227

Complete contact information is available at: https://pubs.acs.org/10.1021/acsanm.4c03577

Author Contributions

○N.M. and U.S. contributed equally to this work. N.M. and U.S. designed and realized the experiments, performed synthesis, characterization, analysis, interpretation, wrote the original draft, reviewed, and edited the final manuscript. S.C., X.Z., and B.A.Z. performed TEM and nano-CT characterization, analysis, reviewed, and edited the final manuscript. D.L. performed synthesis, characterization, and analysis. A.S. performed catalyst synthesis. N.T. performed interpretation, reviewed, and edited the final manuscript. E.S., B.A.Z., M.H., N.V., and P.W. acquired the funding, reviewed, and edited the final manuscript. N.M., U.S., M.H., N.V., and P.W. conceptualized and supervised all the research work. All authors contributed to the discussion and analysis of the results

https://doi.org/10.1021/acsanm.4c03577
ACS Appl. Nano Mater. 2024, 7, 24356−24367

presented and have given approval to the final version of the manuscript.

Notes

The authors declare no competing financial interest.

■ ACKNOWLEDGMENTS

The authors acknowledge financial support from the European Research Council (project 786475: Engineering of Supported Catalytically Active Liquid Metal Solutions) and Deutsche Forschungsgemeinschaft (DFG, German Research Foundation) project-ID 431791331-SFB 1452 and project-ID 416229255-SFB 1411. Sabine Hübner from the Center for Nanoanalysis and Electron Microscopy (CENEM) is acknowledged for her help with FIB cross-section lamella preparation.

■ REFERENCES

(1) Wang, Z.-Y.; He, Z.-H.; Li, L.-Y.; Yang, S.-Y.; He, M.-X.; Sun, Y.-C.; Wang, K.; Chen, J.-G.; Liu, Z.-T. Research progress of CO2 oxidative dehydrogenation of propane to propylene over Cr-free metal catalysts. *Rare Met* **2022**, *41* (7), 2129−2152.

(2) Monai, M.; Gambino, M.; Wannakao, S.; Weckhuysen, B. M. Propane to olefins tandem catalysis: a selective route towards light olefins production. *Chem. Soc. Rev.* **2021**, *50* (20), 11503−11529.

(3) Nawaz, Z. Light alkane dehydrogenation to light olefin technologies: a comprehensive review. *Rev. Chem. Eng.* **2015**, *31* (5), 413−436.

(4) Weckhuysen, B. M.; Schoonheydt, R. A. Alkane dehydrogenation over supported chromium oxide catalysts. *Catal. Today* **1999**, *51* (2), 223−232.

(5) Sattler, J. J. H. B.; Ruiz-Martinez, J.; Santillan-Jimenez, E.; Weckhuysen, B. M. Catalytic Dehydrogenation of Light Alkanes on Metals and Metal Oxides. *Chem. Rev.* **2014**, *114* (20), 10613−10653.

(6) Tan, S.; Gil, L. B.; Subramanian, N.; Sholl, D. S.; Nair, S.; Jones, C. W.; Moore, J. S.; Liu, Y.; Dixit, R. S.; Pendergast, J. G. Catalytic propane dehydrogenation over In2O3−Ga2O3 mixed oxides. *Appl. Catal.* **2015**, *498*, 167−175.

(7) Ashmawy, F. M. Catalytic dehydrogenation of propane on chromia, palladium and platinum supported catalysts. *J. Appl. Chem.* **1977**, *27* (1), 137−142.

(8) Bariås, O. A.; Holmen, A.; Blekkan, E. A. Propane dehydrogenation over supported platinum catalysts: effect of tin as a promoter. *Catal. Today* **1995**, *24* (3), 361−364.

(9) Taccardi, N.; Grabau, M.; Debuschewitz, J.; Distaso, M.; Brandl, M.; Hock, R.; Maier, F.; Papp, C.; Erhard, J.; Neiss, C.; Peukert, W.; Görling, A.; Steinrück, H. P.; Wasserscheid, P. Gallium-rich Pd−Ga phases as supported liquid metal catalysts. *Nat. Chem.* **2017**, *9* (9), 862−867.

(10) Raman, N.; Maisel, S.; Grabau, M.; Taccardi, N.; Debuschewitz, J.; Wolf, M.; Wittkämper, H.; Bauer, T.; Wu, M.; Haumann, M.; Papp, C.; Görling, A.; Spiecker, E.; Libuda, J.; Steinrück, H. P.; Wasserscheid, P. Highly Effective Propane Dehydrogenation Using Ga−Rh Supported Catalytically Active Liquid Metal Solutions. *ACS Catal.* **2019**, *9* (10), 9499−9507.

(11) Raman, N.; Wolf, M.; Heller, M.; Heene-Würl, N.; Taccardi, N.; Haumann, M.; Felfer, P.; Wasserscheid, P. GaPt Supported Catalytically Active Liquid Metal Solution Catalysis for Propane Dehydrogenation−Support Influence and Coking Studies. *ACS Catal.* **2021**, *11* (21), 13423−13433.

(12) Wolf, M.; Raman, N.; Taccardi, N.; Haumann, M.; Wasserscheid, P. Coke Formation during Propane Dehydrogenation over Ga−Rh Supported Catalytically Active Liquid Metal Solutions. *ChemCatChem* **2020**, *12* (4), 1085−1094.

(13) Wolf, M.; Raman, N.; Taccardi, N.; Horn, R.; Haumann, M.; Wasserscheid, P. Capturing spatially resolved kinetic data and coking of Ga−Pt supported catalytically active liquid metal solutions during propane dehydrogenation in situ. *Faraday Discuss.* **2021**, *229* (0), 359−377.

(14) Sebastian, O.; Nair, S.; Taccardi, N.; Wolf, M.; Søgaard, A.; Haumann, M.; Wasserscheid, P. Stable and Selective Dehydrogenation of Methylcyclohexane using Supported Catalytically Active Liquid Metal Solutions − Ga52Pt/SiO2 SCALMS. *ChemCatChem* **2020**, *12* (18), 4533−4537.

(15) Sebastian, O.; Al-Shaibani, A.; Taccardi, N.; Sultan, U.; Inayat, A.; Vogel, N.; Haumann, M.; Wasserscheid, P. Ga−Pt supported catalytically active liquid metal solutions (SCALMS) prepared by ultrasonication − influence of synthesis conditions on n-heptane dehydrogenation performance. *Catal. Sci. Technol.* **2023**, *13* (15), 4435−4450.

(16) Sebastian, O.; Al-Shaibani, A.; Taccardi, N.; Haumann, M.; Wasserscheid, P. Kinetics of dehydrogenation of n-heptane over GaPt supported catalytically active liquid metal solutions (SCALMS). *React. Chem. Eng.* **2024**, *9*, 1154−1163.

(17) Søgaard, A.; de Oliveira, A. L.; Taccardi, N.; Haumann, M.; Wasserscheid, P. Ga−Ni supported catalytically active liquid metal solutions (SCALMS) for selective ethylene oligomerization. *Catal. Sci. Technol.* **2021**, *11* (23), 7535−7539.

(18) Wolf, M.; de Oliveira, A. L.; Taccardi, N.; Maisel, S.; Heller, M.; Khan Antara, S.; Søgaard, A.; Felfer, P.; Görling, A.; Haumann, M.; Wasserscheid, P. Dry reforming of methane over gallium-based supported catalytically active liquid metal solutions. *Commun. Chem.* **2023**, *6* (1), 224.

(19) Raman, N.; Söllner, J.; Madubuko, N.; Nair, S.; Taccardi, N.; Thommes, M.; Haumann, M.; Wasserscheid, P. Top-down vs. bottom-up synthesis of Ga−based supported catalytically active liquid metal solutions (SCALMS) for the dehydrogenation of isobutane. *Chem. Eng. J.* **2023**, *475*, 146081.

(20) Zimmermann, T.; Madubuko, N.; Groppe, P.; Raczka, T.; Dünninger, N.; Taccardi, N.; Carl, S.; Apeleo Zubiri, B.; Spiecker, E.; Wasserscheid, P.; Mandel, K.; Haumann, M.; Wintzheimer, S. Supraparticles on beads for supported catalytically active liquid metal solutions − the SCALMS suprabead concept. *Mater. Horiz.* **2023**, *10* (11), 4960−4967.

(21) Hohner, C.; Kettner, M.; Stumm, C.; Blaumeiser, D.; Wittkämper, H.; Grabau, M.; Schwarz, M.; Schuschke, C.; Lykhach, Y.; Papp, C.; Steinrück, H. P.; Libuda, J. Pt−Ga Model SCALMS on Modified HOPG: Thermal Behavior and Stability in UHV and under Near-Ambient Conditions. *J. Phys. Chem. C* **2020**, *124* (4), 2562−2573.

(22) Carl, S.; Will, J.; Madubuko, N.; Götz, A.; Przybilla, T.; Wu, M.; Raman, N.; Wirth, J.; Taccardi, N.; Zubiri, B. A.; Haumann, M.; Wasserscheid, P.; Spiecker, E. Structural Evolution of GaO_x-Shell and Intermetallic Phases in Ga−Pt Supported Catalytically Active Liquid Metal Solutions. *J. Phys. Chem. Lett.* **2024**, *15*, 4711−4720.

(23) Yamaguchi, A.; Mashima, Y.; Iyoda, T. Reversible Size Control of Liquid-Metal Nanoparticles under Ultrasonication. *Angew. Chem., Int. Ed.* **2015**, *54* (43), 12809−12813.

(24) Wintzheimer, S.; Granath, T.; Oppmann, M.; Kister, T.; Thai, T.; Kraus, T.; Vogel, N.; Mandel, K. Supraparticles: Functionality from Uniform Structural Motifs. *ACS Nano* **2018**, *12* (6), 5093−5120.

(25) Wang, J.; Mbah, C. F.; Przybilla, T.; Apeleo Zubiri, B.; Spiecker, E.; Engel, M.; Vogel, N. Magic number colloidal clusters as minimum free energy structures. *Nat. Commun.* **2018**, *9* (1), 5259.

(26) Wintzheimer, S.; Luthardt, L.; Cao, K. L. A.; Imaz, I.; Maspoch, D.; Ogi, T.; Bück, A.; Debecker, D. P.; Faustini, M.; Mandel, K. M. Multifunctional, Hybrid Materials Design via Spray-Drying: Much more than Just Drying. *Adv. Mater.* **2023**, *35* (47), 2306648.

(27) Vogel, N.; Utech, S.; England, G. T.; Shirman, T.; Phillips, K. R.; Koay, N.; Burgess, I. B.; Kolle, M.; Weitz, D. A.; Aizenberg, J. Color from hierarchy: Diverse optical properties of micron-sized spherical colloidal assemblies. *Proc. Natl. Acad. Sci. U.S.A.* **2015**, *112* (35), 10845−10850.

(28) Goerlitzer, E. S. A.; Klupp Taylor, R. N.; Vogel, N. Bioinspired Photonic Pigments from Colloidal Self-Assembly. *Adv. Mater.* **2018**, *30* (28), 1706654.

https://doi.org/10.1021/acsanm.4c03577
ACS Appl. Nano Mater. 2024, 7, 24356−24367

(29) Han, S. H.; Choi, Y. H.; Kim, S.-H. Co-Assembly of Colloids and Eumelanin Nanoparticles in Droplets for Structural Pigments with High Saturation. *Small* **2022**, *18* (7), 2106048.
(30) Kim, J. H.; Kim, J. B.; Choi, Y. H.; Park, S.; Kim, S.-H. Photonic Microbeads Templated by Oil-in-Oil Emulsion Droplets for High Saturation of Structural Colors. *Small* **2022**, *18* (8), 2105225.
(31) Parker, R. M.; Zhao, T. H.; Frka-Petesic, B.; Vignolini, S. Cellulose photonic pigments. *Nat. Commun.* **2022**, *13* (1), 3378.
(32) Chandler, C. J.; Wilts, B. D.; Brodie, J.; Vignolini, S. Structural Color in Marine Algae. *Adv. Opt. Mater.* **2017**, *5* (5), 1600646.
(33) Wang, J.; Liu, Y.; Bleyer, G.; Goerlitzer, E. S. A.; Englisch, S.; Przybilla, T.; Mbah, C. F.; Engel, M.; Spiecker, E.; Imaz, I.; Maspoch, D.; Vogel, N. Coloration in Supraparticles Assembled from Polyhedral Metal-Organic Framework Particles. *Angew. Chem.* **2022**, *134* (16), 202117455.
(34) Canziani, H.; Bever, F.; Sommereyns, A.; Schmidt, M.; Vogel, N. Roughly Spherical: Tailored PMMA−SiO2 Composite Supraparticles with Optimized Powder Flowability for Additive Manufacturing. *ACS Appl. Mater. Interfaces* **2021**, *13* (21), 25334−25345.
(35) Sultan, U.; Götz, A.; Schlumberger, C.; Drobek, D.; Bleyer, G.; Walter, T.; Löwer, E.; Peuker, U. A.; Thommes, M.; Spiecker, E.; Apeleo Zubiri, B.; Inayat, A.; Vogel, N. From Meso to Macro: Controlling Hierarchical Porosity in Supraparticle Powders. *Small* **2023**, *19* (27), 2300241.
(36) Wang, J.; Schwenger, J.; Ströbel, A.; Feldner, P.; Herre, P.; Romeis, S.; Peukert, W.; Merle, B.; Vogel, N. Mechanics of colloidal supraparticles under compression. *Sci. Adv.* **2021**, *7* (42), No. eabj0954.
(37) Wang, J.; Kang, E.; Sultan, U.; Merle, B.; Inayat, A.; Graczykowski, B.; Fytas, G.; Vogel, N. Influence of Surfactant-Mediated Interparticle Contacts on the Mechanical Stability of Supraparticles. *J. Phys. Chem. C* **2021**, *125* (42), 23445−23456.
(38) Fujiwara, A.; Wang, J.; Hiraide, S.; Götz, A.; Miyahara, M. T.; Hartmann, M.; Apeleo Zubiri, B.; Spiecker, E.; Vogel, N.; Watanabe, S. Fast Gas-Adsorption Kinetics in Supraparticle-Based MOF Packings with Hierarchical Porosity. *Adv. Mater.* **2023**, *35* (44), 2305980.
(39) Zellmer, S.; Garnweitner, G.; Breinlinger, T.; Kraft, T.; Schilde, C. Hierarchical Structure Formation of Nanoparticulate Spray-Dried Composite Aggregates. *ACS Nano* **2015**, *9* (11), 10749−10757.
(40) Barasinski, M.; Schilde, C.; Melzig, S.; Hübner, M.; Garnweitner, G.; Zellmer, S. Micromechanical properties of spray-dried core-shell silica aggregates along with drug release tests. *JCIS Open* **2022**, *6*, 100052.
(41) Yang, Y.; Xiao, J.; Xia, Y.; Xi, X.; Li, T.; Yang, D.; Dong, A. Assembly of CoFe2O4 Nanocrystals into Superparticles with Tunable Porosities for Use as Anode Materials for Lithium-Ion Batteries. *ACS Appl. Nano Mater.* **2022**, *5* (7), 9698−9705.
(42) Wang, Y.; Wise, A. K.; Tan, J.; Maina, J. W.; Shepherd, R. K.; Caruso, F. Mesoporous Silica Supraparticles for Sustained Inner-Ear Drug Delivery. *Small* **2014**, *10* (21), 4244−4248.
(43) Ma, Y.; Cortez-Jugo, C.; Li, J.; Lin, Z.; Richardson, R. T.; Han, Y.; Zhou, J.; Björnmalm, M.; Feeney, O. M.; Zhong, Q.-Z.; Porter, C. J. H.; Wise, A. K.; Caruso, F. Engineering Biocoatings To Prolong Drug Release from Supraparticles. *Biomacromolecules* **2019**, *20* (9), 3425−3434.
(44) Hou, K.; Han, J.; Tang, Z. Formation of Supraparticles and Their Application in Catalysis. *ACS Mater. Lett.* **2020**, *2* (1), 95−106.
(45) Liu, W.; Kappl, M.; Butt, H.-J. Tuning the Porosity of Supraparticles. *ACS Nano* **2019**, *13* (12), 13949−13956.
(46) Li, S.; Liu, J.; Ramesar, N. S.; Heinz, H.; Xu, L.; Xu, C.; Kotov, N. A. Single- and multi-component chiral supraparticles as modular enantioselective catalysts. *Nat. Commun.* **2019**, *10* (1), 4826.
(47) Wooh, S.; Huesmann, H.; Tahir, M. N.; Paven, M.; Wichmann, K.; Vollmer, D.; Tremel, W.; Papadopoulos, P.; Butt, H.-J. Synthesis of Mesoporous Supraparticles on Superamphiphobic Surfaces. *Adv. Mater.* **2015**, *27* (45), 7338−7343.
(48) Pal, N.; Bhaumik, A. Soft templating strategies for the synthesis of mesoporous materials: Inorganic, organic−inorganic hybrid and purely organic solids. *Adv. Colloid Interface Sci.* **2013**, *189*−*190*, 21−41.
(49) Marcos-Hernández, M.; Villagrán, D. 11 - Mesoporous Composite Nanomaterials for Dye Removal and Other Applications. In *Composite Nanoadsorbents: Micro and Nano Technologies*; Kyzas, G. Z., Mitropoulos, A. C., Eds.; Elsevier, 2019; pp 265−293..
(50) Sudo, S.; Nagata, S.; Kokado, K.; Sada, K. Direct Synthesis of Liquid Metal Colloids and Their Transmetalation into Noble Metal Nanoparticles. *Chem. Lett.* **2014**, *43* (8), 1207−1209.
(51) Okamoto, H. Ga-Pt (Gallium-Platinum). *J. Phase Equilib. Diffus.* **2007**, *28* (5), 494.
(52) Bogush, G. H.; Tracy, M. A.; Zukoski, C. F. Preparation of monodisperse silica particles: Control of size and mass fraction. *J. Non-Cryst. Solids* **1988**, *104* (1), 95−106.
(53) Vogel, N.; de Viguerie, L.; Jonas, U.; Weiss, C. K.; Landfester, K. Binary Colloidal Monolayers: Wafer-Scale Fabrication of Ordered Binary Colloidal Monolayers with Adjustable Stoichiometries (Adv. Funct. Mater. 16/2011). *Adv. Funct. Mater.* **2011**, *21* (16), 3064−3073.
(54) Stöber, W.; Fink, A.; Bohn, E. Controlled growth of monodisperse silica spheres in the micron size range. *J. Colloid Interface Sci.* **1968**, *26* (1), 62−69.
(55) Mezhericher, M.; Naumann, M.; Peglow, M.; Levy, A.; Tsotsas, E.; Borde, I. Continuous species transport and population balance models for first drying stage of nanosuspension droplets. *Chem. Eng. J.* **2012**, *210*, 120−135.
(56) Lintingre, E.; Lequeux, F.; Talini, L.; Tsapis, N. Control of particle morphology in the spray drying of colloidal suspensions. *Soft Matter* **2016**, *12* (36), 7435−7444.
(57) Maurice, U.; Mezhericher, M.; Levy, A.; Borde, I. Drying of Droplets Containing Insoluble Nanoscale Particles: Second Drying Stage. *Drying Technol.* **2015**, *33* (15−16), 1837−1848.
(58) Canziani, H.; Chiera, S.; Schuffenhauer, T.; Kopp, S.-P.; Metzger, F.; Bück, A.; Schmidt, M.; Vogel, N. Bottom-Up Design of Composite Supraparticles for Powder-Based Additive Manufacturing. *Small* **2020**, *16* (30), 2002076.
(59) Wirth, J.; Englisch, S.; Drobek, D.; Apeleo Zubiri, B.; Wu, M.; Taccardi, N.; Raman, N.; Wasserscheid, P.; Spiecker, E. Unraveling Structural Details in Ga-Pd SCALMS Systems Using Correlative Nano-CT, 360° Electron Tomography and Analytical TEM. *Catalysts* **2021**, *11* (7), 810.
(60) Hodnik, N.; Zorko, M.; Bele, M.; Hočevar, S.; Gaberšček, M. Identical Location Scanning Electron Microscopy: A Case Study of Electrochemical Degradation of PtNi Nanoparticles Using a New Nondestructive Method. *J. Phys. Chem. C* **2012**, *116* (40), 21326−21333.

https://doi.org/10.1021/acsanm.4c03577
ACS Appl. Nano Mater. 2024, 7, 24356−24367